Document Version
Final published version

Licence
CC BY

Citation (APA)
Natu, A., Araga, M., & HosseinNia, H. (2026). Robust mixed-sensitivity H∞ control synthesis integrating active damping for piezoelectric nanopositioning system under payload-induced uncertainties. *Mechatronics*, *117*, Article 103519. https://doi.org/10.1016/j.mechatronics.2026.103519

Mechatronics 117 (2026) 103519

Contents lists available at ScienceDirect

Mechatronics

journal homepage: www.elsevier.com/locate/mechatronics

Robust mixed-sensitivity H_∞ control synthesis integrating active damping for piezoelectric nanopositioning system under payload-induced uncertainties[☆], [☆☆]

Aditya Natu [*], Manavi Araga, Hassan HosseinNia

Department of Precision and Microsystems Engineering, Delft University of Technology, Mekelweg 2, 2628 CD Delft, The Netherlands

ARTICLE INFO

Keywords:
Robust control
Mixed-sensitivity H_∞ control
Active damping
NRC
Weighting function design
Payload uncertainties
Piezoelectric nanopositioning

ABSTRACT

Piezoelectric nanopositioning systems exhibit low damping and resonance modes that are highly sensitive to loading conditions, resulting in performance degradation under payload variations. Conventional damping and robust control methods typically address these challenges separately, overlooking the coupling between damping and tracking dynamics as well as the influence of higher-order resonant modes. This paper proposes a dual-loop control framework that integrates active damping with mixed-sensitivity H_∞ synthesis to achieve robust reference tracking and disturbance rejection under large resonance frequency variations. A Non-Minimum-Phase Resonant Controller (NRC) is implemented in the inner loop to suppress the dominant resonance and reduce system uncertainty. Generalized plant formulation and systematic weighting design guidelines of arbitrary order are developed to explicitly incorporate higher-order modes in the outer loop H_∞ synthesis. The proposed approach is validated through simulations and experiments on an industrial piezoelectric nanopositioning system, demonstrating improved robustness and precision across the full payload range.

1. Introduction

Nanopositioning systems are widely used in high-precision applications such as microscopy, surface scanning, metrology, and micromanipulation [1]. These systems typically employ piezoelectric actuators due to their high stiffness, large force generation, and sub-nanometre resolution [2]. Flexure-guided mechanisms ensure frictionless motion in micrometre ranges [3], but their low damping introduces multiple high-frequency resonant modes that limit control bandwidth and accuracy. Furthermore, payload variations and piezoelectric hysteresis lead to dynamic changes, prompting the use of various hysteresis compensation techniques [4].

Active damping control is widely adopted to suppress resonances, enhance robustness, and enable higher bandwidths using low-order fixed-structure controllers [5]. Common strategies such as Positive Position Feedback (PPF) [6], Integral Resonance Control (IRC) [7], and Resonant Control (RC) [8] perform well for nominal dynamics but degrade under large resonance variations. Enhanced damping methods, including Robust Resonant Control (RRC) and robust H_∞ control [9,10], improve robustness by reducing plant uncertainty. However, the altered damped dynamics must be considered in the outer loop tracking control to ensure robust performance and disturbance rejection.

Robust control approaches such as H_∞, μ-synthesis, and Linear Quadratic Gaussian (LQG) control have been applied to handle uncertainties from payload variations and actuator nonlinearities [11,12]. A few studies have further integrated active damping with robust tracking control to combine their complementary strengths: achieving high bandwidth, precise tracking, effective disturbance rejection, and robustness to resonance variations [13,14]. For instance, [15] demonstrated a resonant damping controller combined with a mixed-sensitivity H_∞ tracking controller in a MEMS force sensor, providing low-frequency gain shaping and robustness against first-mode resonance variations.

In practice, piezoelectric nanopositioning systems exhibit sharp resonance peaks, with higher-order modes often located near the dominant first mode. These resonances typically fall within the desired control bandwidth, where the first mode limits bandwidth and adjacent modes

---

[☆] This article is part of a Special issue entitled: 'TC 4.2 Mechatronic Systems (IFAC WC 2026)' published in Mechatronics.

[☆☆] This work was financed by Physik Instrumente (PI) SE & Co. KG and co-financed by Holland High Tech with PPS Project supplement for research and development in the field of High Tech Systems and Materials.

[*] Corresponding author.

E-mail addresses: a.m.natu@tudelft.nl (A. Natu), m.araga@tudelft.nl (M. Araga), s.h.hosseinniakani@tudelft.nl (H. HosseinNia).

https://doi.org/10.1016/j.mechatronics.2026.103519
Received 1 November 2025; Received in revised form 16 March 2026; Accepted 19 March 2026

degrade precision by increasing sensitivity to high-frequency reference and disturbance components. While damping controllers effectively suppress the first mode and improve robustness to resonance variations, they generally do not address higher-order modes, relying instead on high-frequency gain roll-off to attenuate unmodelled dynamics. This dependence complicates mixed-sensitivity weight design, as aggressive shaping may lead to unnecessarily high-order or infeasible controllers. To the best of the authors' knowledge, no prior work has explicitly considered the influence of dominant higher-order modes in weight design and robust control synthesis for piezoelectric nanopositioning systems.

This work proposes a mixed-sensitivity H_∞ control synthesis integrated with active damping in a dual closed-loop architecture to achieve robust reference tracking and disturbance rejection under large payload-induced resonance frequency variations. Unlike conventional single-loop architectures or the approach of [15], which allow shaping of only three sensitivity functions, the proposed framework yields five sensitivity functions and enables their simultaneous shaping. The approach is demonstrated on a high-order, lightly damped industrial piezoelectric nanopositioning system. A tamed Non-Minimum-Phase Resonant Controller (NRC) [2] is employed in the inner loop to suppress the dominant resonance and reduce system uncertainty. Thus, this easily tunable, unconventional non-minimum phase controller enables robust damping of the first resonance under large resonance frequency variations. Building on the damped plant model, a systematic framework that incorporates higher-order modes and generalized weighting function design guidelines is developed to enable straightforward mixed-sensitivity H_∞ synthesis via loop shaping. The weighting-function parameters are explicitly linked to system dynamics and closed-loop performance requirements, facilitating an intuitive design process, particularly for piezoelectric nanopositioning systems. The proposed method is validated through comprehensive simulations and experiments, confirming robust performance in both frequency and time domains.

The key contributions of this paper are:

1. Formulation of a generalized plant framework for dual closed-loop architectures, enabling outer loop tracking controller synthesis with a fixed inner loop damping controller.
2. Development of systematic weighting design guidelines for arbitrary weight orders, explicitly accounting for higher-order modes in mixed-sensitivity H_∞ control synthesis.
3. Extensive simulation and experimental validation demonstrating robust reference tracking and disturbance rejection across the full payload range of the nanopositioning system.

The paper is organized as follows: Section 2 outlines the experimental system and identification. Section 3 details the mixed-sensitivity H_∞ control design with active damping and weight design. Section 4 presents simulation results, Section 5 provides experimental validation, and Section 6 concludes the paper.

2. System description and identification

The experimental setup, shown in Fig. 1(a), employs a commercial P-628.1CD PIHera nanopositioner with a 950 μm travel range. The single-axis stage integrates a ceramic-insulated multilayer piezo-stack actuator, a flexure-guided mechanism for frictionless motion, and a high-resolution capacitive displacement sensor for feedback. The stage is driven via a voltage amplifier, and signal-conditioning modules within the modular E-712 piezo-controller. For external control, the hardware interfaces with an NI CompactRIO chassis featuring an embedded FPGA for real-time actuation and 16-bit analog I/O modules for signal transmission and acquisition. The FPGA utilizes a 64-bit double-precision floating-point representation, corresponding to approximately 15 significant decimal digits, which mitigates coefficient quantization and round-off effects. The control algorithm is implemented in LabVIEW, which enables execution of parallel arithmetic operations and deterministic timing governed by the FPGA clock and pipeline structure. The FPGA loop rate is synchronized with the sampling rate to prevent data loss. The actuation range is 0–10 V, with a sampling time $t_s = 30$ μs ($f_s = 33.\overline{33}$ kHz, $f_N = 16.\overline{66}$ kHz), exceeding the frequency range of interest (0–1000 Hz).

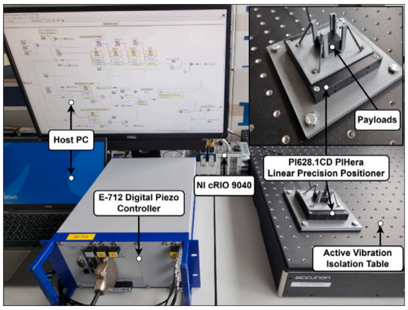

(a) Experimental setup with P-628.1CD PIHera nanopositioner.

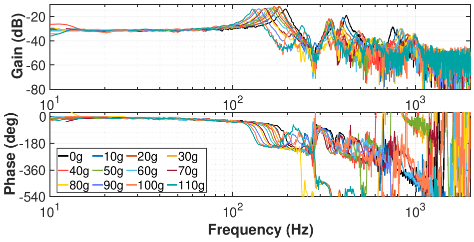

(b) Identified system frequency responses under payload variations.

Fig. 1. System identification for the experimental setup.

To identify the system dynamics, a 0.1 V uniform white noise input with a 0.1 V offset and variance of 0.0033 V^2 was generated in LabVIEW and applied to the actuator. The capacitive sensor output was recorded and analysed in MATLAB, where the frequency response functions (FRFs) were estimated using Chebyshev windowing to reduce spectral leakage. Payload effects were examined using a custom 3D-printed mounting bracket, with masses added in 10 g increments up to 120 g. High coherence and an SNR of approximately 15 dB ensured reliable identification across 0–1000 Hz. The first resonance shifted from 194 Hz to 127 Hz with increasing payload, with similar downward trends in the next three modes (200–1000 Hz), as shown in Fig. 1(b). The phase lag observed below the first resonance is attributed to actuator–amplifier dynamics and inherent delay, while pole–zero interlacing confirms the collocated actuator–sensor configuration.

3. Design methodology

This section outlines the design methodology for synthesizing the mixed-sensitivity H_∞ tracking controller. As introduced in Section 1, the damping controller $C_d(s)$ and the tracking controller $C_t(s)$, together with a linear plant model $G_m(s)$ derived based on system identification data, are integrated into a dual closed-loop architecture (Fig. 2). $C_d(s)$ suppresses the dominant resonant mode in the inner loop, thereby reducing dynamic uncertainty, while the outer loop controller $C_t(s)$ ensures accurate reference tracking. This dual-loop configuration provides robust closed-loop stability and improved noise and disturbance rejection across the operating bandwidth.

Relative uncertainty at the plant level is quantified by comparing the perturbed plant set $G(s)$, arising from payload variations, with the nominal unloaded plant model $G_{n_0}(s)$. To emphasize the advantages of incorporating the active damping controller within the generalized plant structure, the relative uncertainty is also computed considering the perturbed damped plant set $G_d(s)$ relative to the nominal, unloaded

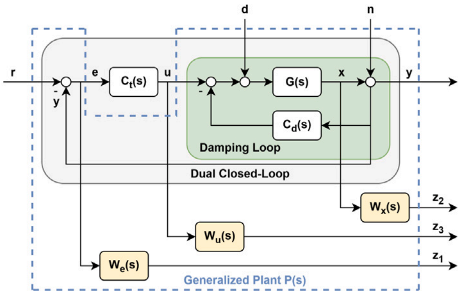

Fig. 2. Block diagram for mixed-sensitivity synthesis in the dual-loop architecture, showing damping and tracking with weighting functions on the regulated outputs.

damped plant $G_{d_0}(s)$. The exogenous inputs r, d, and n denote the reference, input disturbance, and output disturbance (including sensor noise), respectively. The signals y and x represent the measured and actual positions, while e and u denote the tracking error and the control input.

3.1. Sensitivity functions

For the dual closed-loop control architecture shown in Fig. 2, the dual open-loop transfer function is given by:

$$L_D(s) = G(s)\left(C_t(s) + C_d(s)\right). \tag{1}$$

Dual closed-loop stability requires adequate phase margins ϕ_{m_i} at all 0 dB crossovers of $L_D(s)$ [16]:

$$(2k-1)180^\circ \leq \angle L_D(s) \leq (2k+1)180^\circ \text{ when } |L_D(s)| = 0 \text{ dB}, \tag{2}$$

where $k \in \mathbb{Z}$ and $\phi_{m_i} \geq 30^\circ$ typically ensures robustness.

The sensitivity function mapping the output disturbance n to the measured output y is defined as:

$$S_{yn}(s) = \frac{1}{1 + G(s)\left(C_t(s) + C_d(s)\right)} = \frac{1}{1 + L_D(s)}. \tag{3}$$

Similarly, other relevant closed-loop transfer functions are:

$$\begin{aligned}
T_{xr}(s) &= \frac{G(s)C_t(s)}{1 + G(s)\left(C_t(s) + C_d(s)\right)}, & T_{er}(s) &= \frac{1 + G(s)C_d(s)}{1 + G(s)\left(C_t(s) + C_d(s)\right)}, \\
S_{xn}(s) &= \frac{-G(s)\left(C_t(s) + C_d(s)\right)}{1 + G(s)\left(C_t(s) + C_d(s)\right)}, & PS_{yd}(s) &= \frac{G(s)}{1 + G(s)\left(C_t(s) + C_d(s)\right)}, \\
CS_{ur}(s) &= \frac{C_t(s)\left(1 + G(s)C_d(s)\right)}{1 + G(s)\left(C_t(s) + C_d(s)\right)}.
\end{aligned} \tag{4}$$

Tamed NRC is employed as a fixed inner loop damping controller, defined as:

$$C_d(s) = k_d \left(\frac{s - \omega_a}{s + \omega_a}\right)\left(\frac{\omega_l}{s + \omega_l}\right), \tag{5}$$

where k_d and ω_a represent the controller gain and the resonant filter corner frequency, respectively. The parameters are tuned as $k_d = \gamma \cdot |G_{n_0}(0)|^{-1}$ and $\omega_a = n \cdot \omega_{n_0}$, where $G_{n_0}(0)$ and ω_{n_0} denote the DC gain of the nominal unloaded system model and its first resonant frequency.

Owing to its gain–phase decoupling property from the non-minimum-phase characteristic, NRC effectively suppresses the targeted first resonance mode. Its damping performance remains robust to resonance frequency variations when tuned for the nominal unloaded condition [2]. To further mitigate sensor noise feedback and reduce the effect on untargeted higher-order modes, NRC is extended with a first-order low-pass taming filter with a corner frequency ω_l.

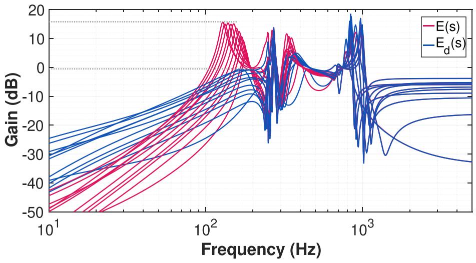

Fig. 3. Multiplicative uncertainty for undamped and damped systems due to payload variations.

3.2. System modelling and uncertainty

Using the identified frequency response data, an 11th-order transfer function model is derived for each measured system response. Given that flexure-based nanopositioning systems are characterized by resonant and anti-resonant modes, and that experimental measurements are conducted at sufficiently low amplitudes within the travel range where the linearity assumption is valid, the plant dynamics are modelled as a linear system composed of a series of resonant and anti-resonant modes.

$$G_m(s) = \underbrace{\frac{\omega_n^2}{s^2 + 2\zeta_n\omega_n s + \omega_n^2}}_{\substack{\text{Dominant} \\ \text{Resonant Dynamics}}} \cdot \underbrace{\prod_{i=2}^{4}\left(\frac{\left(\frac{s}{Z_i}\right)^2 + \left(\frac{2\zeta_{Z_i}s}{Z_i}\right) + 1}{\left(\frac{s}{P_i}\right)^2 + \left(\frac{2\zeta_{P_i}s}{P_i}\right) + 1}\right)}_{\text{Higher-Order Mode Dynamics}} \cdot \underbrace{\frac{g \cdot \omega_A}{s + \omega_A}}_{\substack{\text{Actuator} \\ \text{Amplifier} \\ \text{Dynamics}}} \cdot \underbrace{e^{-\tau s}}_{\text{Delay}}, \tag{6}$$

The four dominant resonant modes are represented by second-order transfer functions, the actuator–amplifier dynamics by a first-order low-pass filter, and the inherent system delay by a second-order Padé approximation. $G_m(s)$ denotes the modelled transfer function capturing the essential dynamic characteristics of the measured system frequency responses, as shown in Fig. 1(b). The parameters ω_n and ζ_n represent the natural frequency and damping ratio of the first dominant mode, respectively. The terms P_i and Z_i correspond to the frequencies of the ith resonance and anti-resonance, with ζ_{P_i} and ζ_{Z_i} denoting their respective damping coefficients. The actuator capacitance and amplifier resistance form a series network introducing a low-pass characteristic with corner frequency ω_A and amplifier gain g, while τ represents the system time delay.

As shown in Fig. 2, $G(s) \in \Pi$ represents the perturbed system models arising from load variations, where Π is the set of all possible perturbed models. These variations are modelled as multiplicative dynamic uncertainties:

$$G(s) = G_{n_0}(s)\left(1 + E(s)\right), \tag{7}$$

where $G_{n_0}(s)$ is the nominal unloaded system frequency response, and $E(s)$ is the complex-valued relative multiplicative uncertainty defined as:

$$E(s) = \left|\frac{G(s) - G_{n_0}(s)}{G_{n_0}(s)}\right|. \tag{8}$$

As illustrated in Fig. 3, the uncertainties are most pronounced near the resonance modes. When the perturbed plant set $G(s)$ is damped using the active damping controller $C_d(s)$, the corresponding uncertainty for the set of damped plants $G_d(s) = \frac{G(s)}{1+G(s)C_d(s)}$ is given by:

$$E_d(s) = \left|\frac{G_d(s) - G_{d_0}(s)}{G_{d_0}(s)}\right|, \tag{9}$$

where $G_{d_0}(s) = \frac{G_{n_0}(s)}{1+G_{n_0}(s)C_d(s)}$ is the nominal damped plant.

As shown in Fig. 3, applying damping control markedly reduces the uncertainty around the first resonance frequency for the set of damped plants. This demonstrates the effectiveness of NRC in fully suppressing the dominant resonance despite frequency variations. The resulting flatness of the uncertainty in this region highlights the robustness of the damping performance. Compared to the undamped case, the reduction in uncertainty is substantial, confirming the dual benefit of improved disturbance rejection and enhanced robustness to dynamic variations.

However, the damping controller has limited influence on uncertainties in untargeted higher-order modes, underscoring the need for a robust outer loop tracking controller to maintain performance across the bandwidth.

3.3. *Mixed-sensitivity H_∞ control synthesis*

Mixed-sensitivity H_∞ synthesis enables simultaneous shaping of multiple sensitivity functions to achieve the desired tracking performance, disturbance rejection, and noise attenuation. Given the exogenous inputs r, d, and n, three outputs can be regulated: the tracking error e, the measured position y, and the actual position x:

$$\begin{aligned} y &= T_{xr}(s)\cdot r + PS_{yd}(s)\cdot d + S_{yn}(s)\cdot n, \\ x &= T_{xr}(s)\cdot r + PS_{yd}(s)\cdot d + S_{xn}(s)\cdot n, \\ e &= T_{er}(s)\cdot r - PS_{yd}(s)\cdot d - S_{yn}(s)\cdot n. \end{aligned} \tag{10}$$

As evident from (4), $S_{yn}(s)$ and $T_{er}(s)$ are inversely related to the tracking controller $C_t(s)$. Thus, at low frequencies, where $C_t(s)$ exhibits high gain, $S_{yn}(s)$ and $T_{er}(s)$ remain small. In contrast, $S_{xn}(s)$ and $T_{xr}(s)$ include $C_t(s)$ in both numerator and denominator terms, leading to $S_{xn}(s) \approx 1$ and $T_{xr}(s) \approx 1$ when the controller gain is high. Consequently, the pairs $(S_{yn}(s), T_{er}(s))$ and $(S_{xn}(s), T_{xr}(s))$ exhibit similar frequency responses, allowing each pair to be shaped effectively through a single weighting function. Therefore, e and x are shaped using the weighting functions $W_e(s)$ and $W_x(s)$, to shape $(S_{yn}(s), T_{er}(s))$ and $(S_{xn}(s), T_{xr}(s))$ respectively. Furthermore, to prevent actuator saturation, u is shaped using $W_u(s)$.

$$u = CS_{ur}(s)\cdot r - C_t(s)\cdot PS_{yd}(s)\cdot d - C_t(s)\cdot S_{yn}(s)\cdot n \tag{11}$$

The generalized plant, with $S(s) = \frac{1}{1+G(s)C_d(s)}$, w.r.t. the control structure depicted in Fig. 2 is:

$$\begin{Bmatrix} z_1 \\ z_2 \\ z_3 \\ e \end{Bmatrix} = \underbrace{\begin{bmatrix} W_e(s) & -W_e(s)G(s)S(s) & -W_e(s)S(s) & -W_e(s)G(s)S(s) \\ 0 & W_x(s)G(s)S(s) & -W_x(s)C_d(s)G(s)S(s) & W_x(s)G(s)S(s) \\ 0 & 0 & 0 & W_u(s) \\ 1 & -G(s)S(s) & -S(s) & -G(s)S(s) \end{bmatrix}}_{P(s)} \begin{Bmatrix} r \\ d \\ n \\ u_1 \end{Bmatrix} \tag{12}$$

A lower Linear Fractional Transformation (LFT) between the generalized plant $P(s)$ and the tracking controller $C_t(s)$ is performed to derive the closed-loop relationship between the regulated outputs and the exogenous inputs:

$$N = F_l\left(P(s), C_t(s)\right) = \begin{bmatrix} T_{er}(s) & -PS_{yd}(s) & -S_{yn}(s) \\ T_{xr}(s) & PS_{yd}(s) & S_{xn}(s) \\ CS_{ur}(s) & -C_t(s)\cdot PS_{yd}(s) & -C_t(s)\cdot S_{yn}(s) \end{bmatrix}. \tag{13}$$

Thus, the objective of the mixed-sensitivity H_∞ control synthesis is:

$$\min_{C_t(s)} \left\| N(C_t(s)) \right\|_\infty , \tag{14}$$

with the specification for the synthesis given by:

$$\|N\|_\infty = \max_\omega \overline{\sigma}\left(N(j\omega)\right) = \gamma \le 1. \tag{15}$$

Remark 1. Simultaneous shaping of the sensitivity pairs $(S_{yn}(s), T_{er}(s))$ and $(S_{xn}(s), T_{xr}(s))$ is enabled by the strategic selection of e and x as regulated outputs. Alternative choices can force a single weighting function to govern mismatched sensitivity pairs. For example, selecting y as a regulated output would require shaping $(S_{yn}(s), T_{xr}(s))$, which have distinct frequency responses and thus conflicting shaping requirements.

Remark 2. The dual-loop architecture in Fig. 2 can be simplified to a single-loop by using a single, composite controller $C_d(s) + C_t(s)$. This reduces the scale of the problem, as only three sensitivities must be shaped. However, this necessitates a non-intuitive weighting-function design to synthesize the composite controller. This challenge is exacerbated by the fact that a tamed NRC exploits its non-minimum-phase characteristics for robust inner loop damping. Implementing a dual-loop architecture that synthesizes $C_d(s)$ with similar properties as tamed NRC would require an unorthodox weighting function design approach, especially since standard H_∞ synthesis algorithms typically avoid non-minimum phase solutions. The proposed methodology in Section 3.3 overcomes this challenge by incorporating the tamed NRC within the generalized plant as the active damping controller, enabling the adoption of the conventional weighting function design approach for the design of outer loop tracking controller.

3.4. *Weighting function design guidelines*

The weighting function $W_e(s)$ that shapes the tracking error e has the form:

$$W_e(s) = \frac{1}{\prod_{i_e=1}^{n_e} M_{e_{i_e}}} \prod_{i_e=1}^{n_e} \left(\frac{s + M_{e_{i_e}}\omega_{e_{i_e}}}{s + A_{e_{i_e}}\omega_{e_{i_e}}} \right), \tag{16}$$

where n_e denotes the order of the weighting function $W_e(s)$, corresponding to the number of integrators required for tracking control. $\prod_{i_e=1}^{n_e} M_{e_{i_e}}$ defines the high-frequency bound or the sensitivity function maxima. The characteristic equation of the dual closed-loop system is $1 + L_D(s)$, analogous to that of a single-loop system. Hence, the Nyquist stability criterion for a dual-loop configuration can be evaluated using the dual open-loop transfer function $L_D(s)$. Therefore, $\prod_{i_e=1}^{n_e} M_{e_{i_e}}$ serves as a measure of the minimum distance from the critical point $(-1, 0)$ or the modulus margin for stability. $\prod_{i_e=1}^{n_e} A_{e_{i_e}}$ specifies the low-frequency bound and should be chosen below the steady-state error requirement. When this criterion is unknown a priori, setting $\prod_{i_e=1}^{n_e} A_{e_{i_e}} \le 0.01 \cdot \mathcal{R}$, where $\mathcal{R}$ is the system resolution, typically yields satisfactory results. $\omega_{e_{i_e}}$ imposes that the first 0 dB crossover of $L_D(s)$ must occur at or beyond $\omega_{e_{i_e}}$. $\omega_{e_{i_e}}$ can also be associated with the integrator cut-off frequency for the tracking controller and must be selected such that the phase lag from the integrator(s) does not adversely affect the phase margin of L_D. Choosing excessively high $\omega_{e_{i_e}}$ may require a high integrator cut-off, reducing stability margins, particularly in the presence of system delays. Typically, selecting $\omega_{e_{i_e}} \in [0.05,\ 0.1]\omega_n$, where ω_n is the first resonance, yields satisfactory performance.

Remark 3. Although setting $\prod_{i_e=1}^{n_e} A_{e_{i_e}} \approx \mathcal{R}$ theoretically provides the lowest achievable steady-state error, it was observed that this choice causes the synthesis process to be dominated by the associated constraint, resulting in suboptimal performance with respect to other design objectives. A more balanced design is achieved by selecting $\prod_{i_e=1}^{n_e} A_{e_{i_e}} \le 0.01 \cdot \mathcal{R}$.

The weighting function $W_x(s)$, shaping the actual position x is given by:

$$W_x(s) = \frac{1}{\prod_{i_x=1}^{n_x} A_{x_{i_x}}} \prod_{i_x=1}^{n_x} \left(\frac{s + \omega_{x_{i_x}}}{s + \left(M_{x_{i_x}} / A_{x_{i_x}} \right) \cdot \omega_{x_{i_x}}} \right). \tag{17}$$

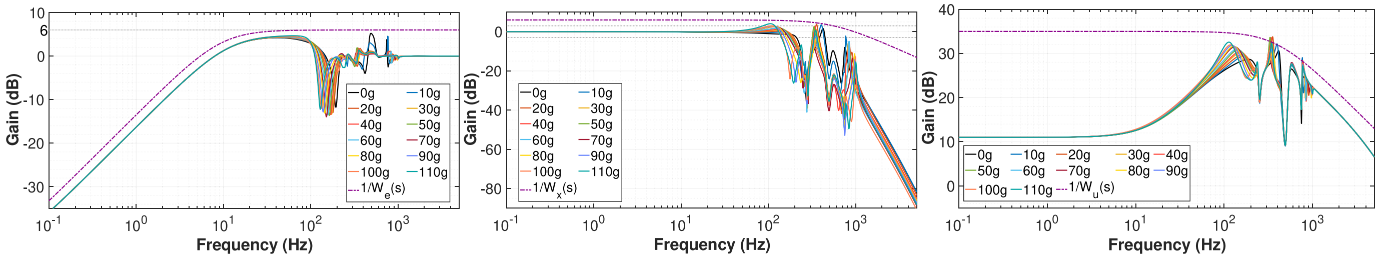

(a) $S_{yn}(s)$ ($n_e = 1$, $A_e = 5 \cdot 10^{-3}$, $M_e = 6$ dB, $\omega_e \approx 5$ Hz)
(b) $T_{xr}(s)$ ($n_x = 1$, $A_x = 10^{-4}$, $M_x = 6$ dB, $\omega_x \approx 557$ Hz)
(c) $CS_{ur}(s)$ ($n_u = 1$, $A_u = 10^{-3}$, $M_u = 35$ dB, $\omega_u \approx 478$ Hz)

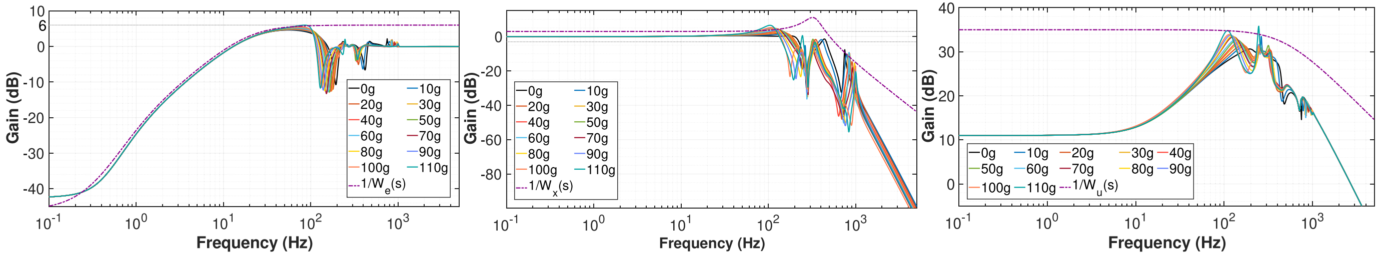

(d) $S_{yn}(s)$ ($n_e = 3$, $A_{e_{tot}} = 5 \cdot 10^{-3}$, $M_{e_{tot}} = 6$ dB, $\omega_e \approx 2$ Hz)
(e) $T_{xr}(s)$ ($n_x = 2$, $A_{x_{tot}} = 10^{-4}$, $M_{x_{tot}} = 6$ dB, $\omega_x \approx 334$ Hz)
(f) $CS_{ur}(s)$ ($n_u = 1$, $A_u = 10^{-3}$, $M_u = 35$ dB, $\omega_u \approx 478$ Hz)

Fig. 4. Frequency response for $S_{yn}(s)$, $T_{xr}(s)$, and $CS_{ur}(s)$ with first-order weights (a–c) and higher-order weights (d–f).

n_x denotes the order of the $W_x(s)$, determining the high-frequency roll-off rate. $\prod_{i_x=1}^{n_x} M_{x_{i_x}}$ denotes the low-frequency bound and is associated with reference-tracking performance. Since a response of $x/r \approx 1$ is desired for motion tracking applications, it should be selected as close to 0 dB as possible. $\prod_{i_x=1}^{n_x} A_{x_{i_x}}$ defines the high-frequency bound or the minima of the sensitivity function. $\prod_{i_x=1}^{n_x} A_{x_{i_x}} \in [0.5, 1] \cdot \mathcal{R}$ may be used, as outputs near the measurement resolution are not physically meaningful. $\omega_{x_{i_x}}$ represent the corner frequency of high-frequency roll-off and should be chosen near the higher-order modes. This minimizes amplification at higher-order resonances and mitigates the influence of model uncertainties, which usually increase with frequency.

The structure in (17) can also be applied to shape u, with the low-frequency bound chosen as $\prod_{i_u=1}^{n_u} M_{u_{i_u}} \leq \frac{u_s}{r_{max}}$ to ensure that the control effort is within actuator limits. Here, r_{max} denotes the maximum expected reference amplitude, and u_s represents the actuator saturation limit.

Sensitivity analyses were conducted to examine the relationship between weighting function parameters and synthesis results (see Fig. 5). Since three outputs are regulated simultaneously, resulting in the concurrent shaping of multiple sensitivities, variations in a single weighting parameter influence the overall synthesis rather than only the associated sensitivity. Nevertheless, a strong correlation was observed between the corner frequency $\omega_{e_{i_e}}$ of the weighting function $W_e(s)$ and the integrator cut-off for the synthesized tracking controller, with decreasing $\omega_{e_{i_e}}$ leading to a lower cut-off. A limited degree of correlation was also identified between the corner frequency $\omega_{x_{i_x}}$ of $W_x(s)$ and the high-frequency roll-off, whereby decreasing $\omega_{x_{i_x}}$ results in increased roll-off. Finally, it should be noted that imposing more stringent low- and high-frequency weighting bounds ($A_{e_{i_e}}$, $M_{x_{i_x}}$ and $M_{e_{i_e}}$, $A_{x_{i_x}}$ respectively) reduces the feasible solution space for controller synthesis and may lead to suboptimal designs.

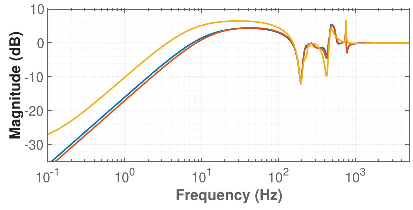

(a) $S_{yn}(s)$ with variation in ω_e

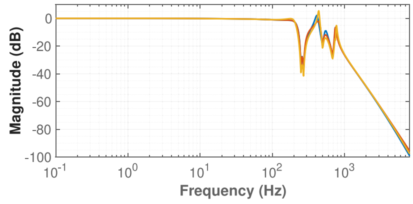

(b) $T_{xr}(s)$ with variation in ω_x

Fig. 5. Sensitivity of $S_{yn}(s)$ and $T_{xr}(s)$ to variations in ω_e and ω_x, respectively. (🟦) represents original parameters, while (🟧) and (🟨) correspond to a 20% increase and 20% decrease, respectively.

4. Simulations

Two sets of weighting functions were designed using the proposed guidelines. The first set, comprising first-order weights, offers greater design flexibility and accommodates variations in plant dynamics due to payload changes. The second set employs higher-order weights to maximize nominal performance with limited consideration for robustness. The results for both designs are compared under nominal and off-nominal payloads (see Fig. 4). The synthesis yields $\gamma_{\text{first-order}} = 1.15$ and $\gamma_{\text{higher-order}} = 1.44$. These values do not satisfy (15). However, in mixed-sensitivity H_∞ synthesis with multiple regulated outputs, satisfactory performance is achieved if the maximum singular value, of each individual row of the closed-loop transfer function $N(s) = \texttt{lft}(P(s), C_l(s))$ does not exceed unity:

$$\max_{\omega} \overline{\sigma}(N_i(j\omega)) \leq 1 \text{ for all rows } N_i \text{ of } N. \tag{18}$$

Both weighting strategies meet this condition, with minor localized violations at higher-order resonant modes, indicating acceptable syntheses (see Fig. 6).

For the nominal unloaded system, higher-order weights yield superior performance compared to the first-order weights, achieving improved tracking and disturbance rejection through increased low-frequency gain (0.1–100 Hz), faster high-frequency roll-off to mitigate

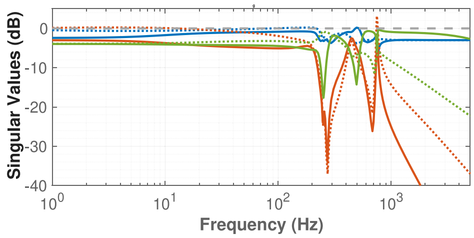

Fig. 6. $\max_{\omega} \bar{\sigma}(N_i(j\omega))$. Solid and dotted lines denote first-order higher-order weighting functions respectively; $i = 1$ using (🟦), $i = 2$ using (🟧), $i = 3$ using (🟩).

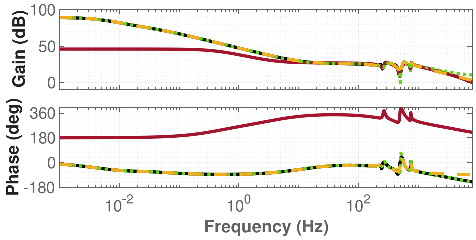

Fig. 7. 37th-order controller obtained via H_∞ synthesis (▬); ROM obtained via NCF method (🟥), balanced truncation method (···) and `ssest` (- - -).

higher-order resonances and model uncertainties, and a wider ±3 dB bandwidth.

However, under off-nominal conditions, the stringent higher-order weighting restricts sensitivity compliance and limits robustness to narrow variations in the plant. In contrast, first-order weights provide greater flexibility, ensuring robust performance across a wider range of uncertainty. Given the significant plant variations in this application, experiments employ the controller synthesized with first-order weights. Under high mass loading, $CS_{ur}(s)$ slightly exceeds its specified bound, but since these deviations are localized beyond the control bandwidth, remain below the actuator limits, and all other sensitivity criteria are satisfied, the design is deemed robust and acceptable.

Remark 4. Higher-order weighting functions are recommended for systems with a smaller relative uncertainty in their dominant resonant modes, especially under stringent requirements for bandwidth achieved, low-frequency reference tracking, and disturbance rejection.

5. Experimental results

This section presents experimental validation of the design and simulations from Sections 3 and 4, using the controller designed using first-order weighting functions. Closed-loop performance is evaluated in the frequency and time domains under nominal and non-nominal payloads.

5.1. Controller implementation

Using first-order weighting functions, a 37th-order controller was synthesized. For practical implementation, reduced-order models (ROMs) were investigated using Hankel-norm-based techniques, such as balanced truncation and normalized coprime factor (NCF) methods, as well as the predictive error minimization approach via MATLAB's `ssest` function (see Fig. 7). For a 9th-order ROM, the NCF method failed to adequately capture the low-frequency dynamics. A comparison was made between balanced truncation and predictive error minimization by evaluating the error $E_{ROM} = C_t^{\mathrm{ROM}}(s) - C_t(s)$. It was observed that in the frequency range with the dominant plant dynamics (50–1000 Hz), the ROM obtained using `ssest` exhibited a smaller error. This 9th-order `ssest`-based ROM achieved a NRMSE fitness of 99.98%. Furthermore, the reduction in controller order was found to have a negligible impact on the level of H_∞ synthesis performance γ. This ROM was discretized using the bilinear (Tustin) transform and implemented on the FPGA.

5.2. Frequency response and robustness analysis

The 9th-order ROM of the synthesized tracking controller was implemented in the dual closed-loop configuration and experimentally evaluated under varying payloads (see Fig. 8). For payloads up to 60 g, the ±3 dB bandwidth remained above the first resonance (Table 1), consistent with the simulation results. At higher payloads, slight deviations from predictions were observed, primarily due to system nonlinearities and payload-induced variations in mode shape. While achieving a ±3 dB bandwidth close to or exceeding the first resonant frequency is not a strict design requirement, prior work has demonstrated that such performance is attainable using the dual-loop architecture with NRC for active damping [2,16]. Consequently, ±3 dB bandwidth $\gtrapprox$ 1st resonance was considered an implicit performance metric during controller synthesis.

Robust stability of the dual-loop system requires a phase margin $\phi_{m_i} \geq 30°$ at each 0 dB crossing of $L_D(s)$, as defined in Section 3.1. The phase margins and crossover frequencies, summarized in Table 1, show $\phi_{m_i} \geq 40°$ for all cases, confirming that the synthesized mixed-sensitivity H_∞ controller maintains robust stability and compliance with the designed weighting specifications across all payload conditions.

5.3. Reference tracking and disturbance rejection performance

Piezoelectric systems are widely used in raster-scanning applications. Therefore, reference tracking performance was evaluated using a triangular input. Owing to the periodic nature of triangular waveforms, they can be decomposed into sinusoids of the fundamental frequency and its odd harmonics, providing a direct and intuitive link to the effective closed-loop tracking bandwidth. The tracking responses for varying payloads (Fig. 9) and RMS errors (Table 2) confirm consistent performance across all loading conditions. RMS errors remain low at low frequencies but increase beyond 50 Hz, despite the ±3 dB bandwidth extending well beyond this range. This degradation corresponds to deviations in $T_{xr}(s)$, attributed to unmodelled actuator hysteresis and higher-order harmonics of the triangular reference. Incorporating hysteresis compensation could further improve tracking accuracy.

Disturbance rejection was evaluated through step-tracking experiments with external disturbances. A step input of 8 μ m was applied while introducing a chirp disturbance, with a frequency sweep of 50 Hz to 250 Hz (amplitude $= 0.8$ μm, variance $= 0.2$ μm^2). As shown in Fig. 10, the controller maintains effective disturbance rejection across all payloads across the frequency sweep of the chirp disturbance. The effect of the disturbance is attenuated and can be seen as a low magnitude sinusoidal variations in the steady-state sensor output. This behaviour is consistent with the process sensitivity (Fig. 8(e)), which remains of low (well below 0 dB) and nearly constant magnitude within this frequency range. Additionally, transients associated with the onset of the chirp disturbance are not clearly observable due to the limited resolution of the analog modules. Comparable performance was observed under a uniform white noise (maximum amplitude $=$ 0.8 μm, variance $= 0.2$ μm^2). The robustness of disturbance rejection performance under varying payload conditions was further quantified by computing the variance of the position output. Similar variance values (≈ 0.008 μm^2) were obtained during step tracking with disturbance inputs, irrespective of the disturbance type or mass loading.

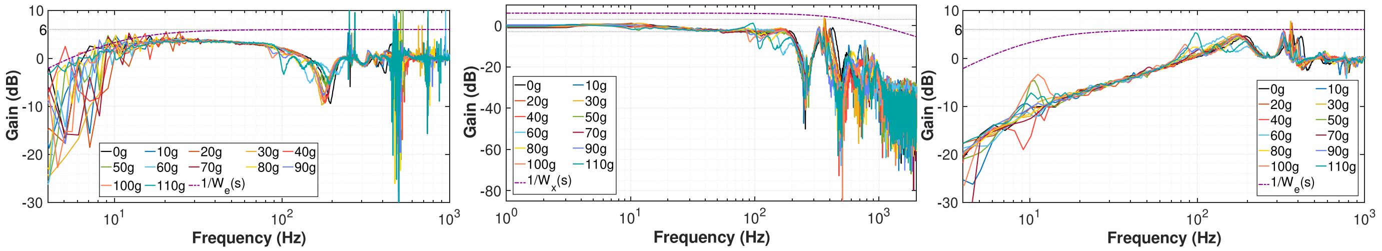

(a) $S_{yn}(s)$ (b) $T_{xr}(s)$ (c) $T_{er}(s)$

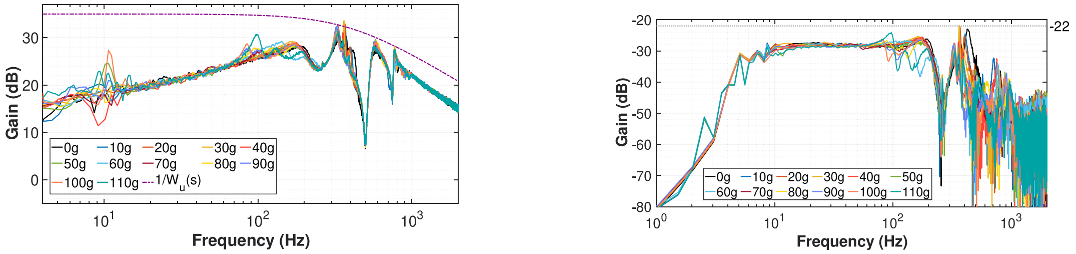

(d) $CS_{ur}(s)$ (e) $PS_{yd}(s)$

Fig. 8. Experimental frequency responses of $S_{yn}(s)$, $T_{xr}(s)$, $T_{er}(s)$, $CS_{ur}(s)$ and $PS_{yd}(s)$ under varying payloads.

Table 1
Frequency domain performance under varying payloads.

Load case	1st Res. (Hz)	±3 dB BW (Hz)	Phase Margin, ϕ_{m_i} (deg)			Crossover frequency (Hz)		
0 g	194	197	51	108	114	8.5	176	207
10 g	179	184	49	100	118	8.4	164	195
20 g	179	188	47	97.7	116	8.4	161	196
30 g	173	181	40	98.1	120	8.4	156	190
40 g	169	184	50	99.1	121	8.4	161	197
50 g	163	176	53	129	171	8.4	175	191
60 g	157	145	52	–	–	8.4	–	–
70 g	151	103	52	109	137	8.4	167	195
80 g	144	97	50	116	128	8.4	167	192
90 g	138	86	49	111	129	8.4	164	191
100 g	132	85	42	106	127	8.3	162	190
110 g	128	102	52	–	–	8.3	–	–

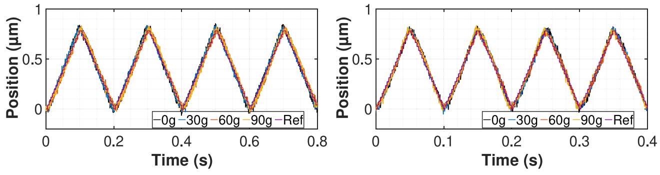

(a) 5 Hz (b) 10 Hz

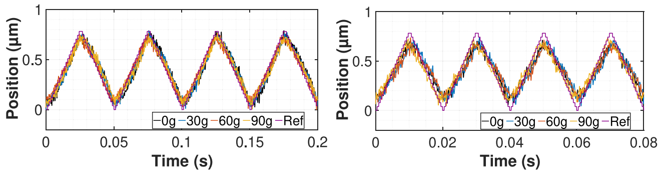

(c) 20 Hz (d) 50 Hz

Fig. 9. Triangular reference tracking with different frequencies for varying payloads.

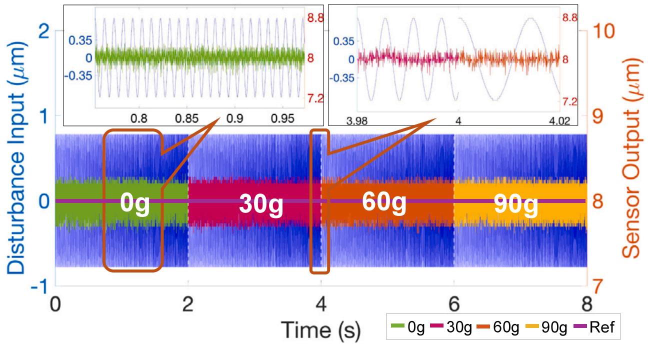

Fig. 10. Step tracking under chirp disturbance for varying payloads.

6. Conclusion

This work presented a dual closed-loop control strategy integrating active damping with mixed-sensitivity H_∞ synthesis for robust control of high-order, lightly damped piezoelectric nanopositioning systems. A Non-Minimum-Phase Resonant Controller suppresses the dominant resonance and enables systematic robust control synthesis by reducing uncertainty. The proposed generalized plant framework and weighting design guidelines incorporate higher-order modes, ensuring robustness and performance without excessive controller complexity. Experiments demonstrate consistent reference tracking and disturbance rejection across varying payloads, establishing a practical and scalable approach for robust nanopositioning control. Future work will focus on incorporating modelling structured uncertainties for μ-synthesis-based control to establish formal robustness margins, albeit with potential increases in design complexity and controller order.

Table 2
RMS tracking error e_{RMS} (in μm) for different frequencies and loading conditions.

Load case	1 Hz	5 Hz	10 Hz	20 Hz	50 Hz	75 Hz	100 Hz	150 Hz
0 g	0.02	0.05	0.08	0.12	0.17	0.20	0.23	0.31
10 g	0.02	0.05	0.08	0.12	0.17	0.20	0.24	0.33
20 g	0.02	0.04	0.08	0.11	0.17	0.20	0.25	0.36
30 g	0.02	0.05	0.08	0.12	0.17	0.20	0.25	0.38
40 g	0.02	0.05	0.08	0.12	0.18	0.20	0.25	0.36
50 g	0.06	0.08	0.10	0.13	0.18	0.22	0.27	0.42
60 g	0.03	0.05	0.08	0.12	0.19	0.20	0.25	0.36
70 g	0.03	0.05	0.09	0.12	0.19	0.20	0.25	0.35
80 g	0.06	0.08	0.10	0.13	0.18	0.22	0.27	0.34
90 g	0.04	0.06	0.08	0.12	0.18	0.22	0.25	0.36
100 g	0.07	0.09	0.11	0.14	0.19	0.24	0.24	0.39
110 g	0.07	0.09	0.11	0.14	0.18	0.26	0.26	0.33

CRediT authorship contribution statement

Aditya Natu: Writing – review & editing, Writing – original draft, Visualization, Validation, Supervision, Project administration, Methodology, Investigation, Formal analysis, Conceptualization. **Manavi Araga:** Writing – review & editing, Writing – original draft, Visualization, Validation, Software, Project administration, Methodology, Investigation, Formal analysis, Data curation, Conceptualization. **Hassan HosseinNia:** Writing – review & editing, Validation, Supervision, Resources, Investigation, Funding acquisition, Conceptualization.

Declaration of competing interest

The authors declare that they have no known competing financial interests or personal relationships that could have appeared to influence the work reported in this paper.

Data availability

Data will be made available on request.

References

[1] Ding B, Li X, Li C, Li Y, Chen S-C. A survey on the mechanical design for piezo-actuated compliant micro-positioning stages. Rev Sci Instrum 2023;94(10).

[2] Natu A, HosseinNia H. Non-minimum-phase resonant controller for active damping control: application to piezo-actuated nanopositioning system. Control Eng. Pract. 2026;169:106790.

[3] Yong Y, Moheimani SR, Kenton BJ, Leang K. Invited review article: High-speed flexure-guided nanopositioning: Mechanical design and control issues. Rev Sci Instrum 2012;83(12).

[4] Yuan Z, Zhou S, Zhang Z, Xiao Z, Hong C, Chen X, Zeng L, Li X. Piezo-actuated smart mechatronic systems: Nonlinear modeling, identification, and control. Mech Syst Signal Process 2024;221:111715.

[5] Chen Z, Zhong X, Shi J, Zhang X. Damping-enabling technologies for broadband control of piezo-stages: A survey. Annu Rev Control 2021;52:120–34.

[6] Preumont A. Vibration control of active structures: an introduction. Springer; 2002.

[7] Feng H, Pang A, Zhou H. High precision robust control design of piezoelectric nanopositioning platform. Sci Rep 2022;12(1):10357.

[8] Das SK, Pota HR, Petersen IR. A MIMO double resonant controller design for nanopositioners. IEEE Trans Nanotechnol 2014;14(2):224–37.

[9] Ling J, Rakotondrabe M, Feng Z, Ming M, Xiao X. A robust resonant controller for high-speed scanning of nanopositioners: Design and implementation. IEEE Trans Control Syst Technol 2019;28(3):1116–23.

[10] Aphale SS, Ferreira A, Moheimani SR. A robust loop-shaping approach to fast and accurate nanopositioning. Sensors Actuators A: Phys 2013;204:88–96.

[11] Ahmad I, Ali MA, Ko W. Robust μ-synthesis with dahl model based feedforward compensator design for piezo-actuated micropositioning stage. IEEE Access 2020;8:141799–813.

[12] Habibullah H, Pota HR, Petersen I. A robust control approach for high-speed nanopositioning applications. Sensors Actuators A: Phys 2019;292:137–48.

[13] Yang C, Youcef-Toumi K. Decoupled tracking and damping control of piezo-actuated nanopositioner enabled by multimode charge sensing. Mech Syst Signal Process 2022;173:109046.

[14] Feng H, Zhou H, Jiang C, Pang A. High precision structured H_∞ control of a piezoelectric nanopositioning platform. Plos One 2023;18(6):e0286471.

[15] Dadkhah D, Moheimani SR. Combining H_∞ and resonant control to enable high-bandwidth measurements with a MEMS force sensor. Mechatronics 2023;96:103086.

[16] Natu AM, HosseinNia H. Non-minimum-phase based loop shaping for multimode active damping control: Application to piezoelectric nanopositioning system. 2025, Available At SSRN 5588813.